

Nonlinear Non-Hermitian Skin Effect and Skin Solitons in Temporal Photonic Feedback Lattices

Shulin Wang^{1,2}, Bing Wang^{1,*}, Chenyu Liu¹, Chengzhi Qin¹, Lange Zhao¹, Weiwei Liu¹, Stefano Longhi^{3,4,*}, and Peixiang Lu^{1,5,*}

¹Wuhan National Laboratory for Optoelectronics and School of Physics, Huazhong University of Science and Technology, Wuhan 430074, China.

²School of Physics, Southeast University, Nanjing 211189, China.

³Dipartimento di Fisica, Politecnico di Milano, Piazza Leonardo da Vinci 32, I-20133 Milano, Italy.

⁴IFISC (UIB-CSIC), Instituto de Física Interdisciplinar y Sistemas Complejos, E-07122 Palma de Mallorca, Spain.

⁵Hubei Key Laboratory of Optical Information and Pattern Recognition, Wuhan Institute of Technology, Wuhan 430205, China.

*Corresponding authors:

B. W. (email: wangbing@hust.edu.cn),

S. L. (email: stefano.longhi@polimi.it),

P. L. (email: lupeixiang@hust.edu.cn).

Abstract

Non-Hermitian skin effect (NHSE), i.e., the localization of eigenstates near lattice boundaries, has recently spurred tremendous interest in topological physics. Beyond the well-explored linear NHSE, the interplay of nonlinearity and skin localization represents a cutting-edge area of research, offering novel insights into wave propagation and localization control in various physical systems. Unlike the linear NHSE successfully observed in weak-power optical systems, the observation of nonlinear NHSE and resulting ‘skin solitons’ remains so far elusive, mainly due to the high energy levels required in most of nonlinear effects. Here we report the experimental demonstration of nonlinear NHSE in a Kerr nonlinear temporal photonic lattice, where the high-power limitation and lack of tunability intrinsic to optical materials are overcome by an artificial nonlinearity arising from opto-electronic feedback. Thanks to Kerr self-trapping, the nonlinear NHSE is demonstrated to possess much better localization strength and robustness at the preferred boundary compared to the linear case. Away from the preferred boundary, Kerr self-trapping can even inhibit NHSE-induced transport and form stable skin solitons. Harnessing the nonlinearity-controlled NHSE, we judiciously design an optical router with a flexibly-tuned output port. Our findings promise great applications in robust signal transmission, routing, and processing.

Non-Hermitian (NH) physics has garnered significant attention over the past two decades due to its distinctive properties, which stand in stark contrast to those of traditional Hermitian systems¹⁻⁴. Unlike Hermitian systems, which are characterized by real eigenvalue spectra and time-reversible dynamics, NH systems can exhibit complex eigenvalues, leading to phenomena such as non-reciprocal wave propagation, exceptional points, and non-Hermitian skin effect (NHSE). These unique behaviors have opened up new avenues of research and potential applications, particularly in areas such as photonics, quantum mechanics, and condensed matter physics. The NHSE is perhaps one of the most intriguing phenomena in this exciting field⁵⁻⁹. The NHSE describes the localized behaviors of eigenstates near preferred edges in a lattice with asymmetric hoppings and open boundaries, which remarkably differs from the extended Bloch waves in the Hermitian case. Due to the NHSE, the traditional bulk-boundary correspondence fails to predict the topological transition and needs to be revised, which has recently evoked the rapid development of NH topological physics. Beyond the above physical innovations, the intrinsic localization of NHSE and its sensitivity on boundary condition host important applications in energy harvesting¹⁰ and quantum sensing^{11,12}. Optical system is considered as a fantastic platform to observe the NHSE and implement its application^{10,13-15}. Utilizing the temporal quantum-walk lattice emerging from two coupled fiber loops with gain and loss, the NHSE under domain-wall boundary condition was realized and applied for topological light funneling¹⁰.

Despite the above successes, nearly all previous studies on NHSE were performed in the linear regime. The interplay of nonlinearity and skin localization provides a promising frontier of research, combining some key concepts of nonlinear physics such as solitons and NH topology of linear lattice systems, paving the way toward new ways for wave localization control and management. Until quite recently, only a few works shed light on the nonlinear NHSE¹⁶⁻²², predicting the competition between nonlinear localization in the bulk and skin effect, the existence and stability of nonlinear skin solitons²² both at system edges and bulk. Nevertheless, research on nonlinear NHSE and its potential applications is still in its early stages, with experimental demonstrations of nonlinear NHSE and skin solitons yet to be realized.

In this work we report on the first experimental demonstration of the Kerr nonlinear NHSE and skin solitons in a nonlinear optical system employing a synthetic Kerr nonlinear temporal lattice. To overcome high-power requirements and the lack of tunable nonlinearity in typical nonlinear optical setups²³⁻²⁷, in our experiment we introduce artificial tunable nonlinearity arising from opto-electronic

feedback. We demonstrate skin solitons both at edges and in bulk at high nonlinearities. Under phase disorder, we also show the stability and enhanced robustness of nonlinear skin modes as compared to their linear counterpart. Inspired by the nonlinear control of NHSE, we design a light router with its output port flexibly tuned by nonlinear strength. Our study offers a framework to explore and harness the interplay of NH topology and nonlinear effect in unprecedented ways, with potential applications in robust optical signal transmission, routing, and processing.

Results

Construction of Kerr nonlinear NH temporal lattice. A synthetic temporal lattice can be established from two coupled fiber loops. As diagrammed in Fig. 1a, the two loops have slightly different lengths and are bridged by a variable optical coupler (VOC). The average time delay and time delay difference of the two loops are T and $2\Delta T$, respectively. When a light pulse passes through VOC, it splits into two parts and enters different loops. The parts circulating in the short and long loops relatively acquire a time advance $-\Delta T$ and a time delay ΔT compared to the averaging circulation time T , as shown in Fig. 1b where t is the real time axis, m is the circulation number in a single loop. By encoding the time slots of pulses within an identical circulation into integers, we can obtain a series of discrete sites n and thus construct a lattice model in time domain^{10,15,25-27}, as shown in Fig. 1c. Moreover, the circulation number acts as the evolution dimension m of lattice. The pulse circulations in short and long loops correspond to the leftwards and rightwards hoppings in the lattice. To realize the nonreciprocal hoppings and open boundary condition (OBC) essential for NHSE, we introduce loss/gain modulation and dynamically-controlled coupling into two loops. The gain factors in leftwards and rightwards hoppings are denoted as $e^{-\gamma}$ and e^{γ} , respectively. The sets of available sites under OBC are chosen as $\{-N, -(N-2), \dots, N-2, N\}$ and $\{-(N+1), -(N-1), \dots, N-1, N+1\}$ in the even and odd steps, where N is a positive even integer. The experimental setup and OBC construction are elucidated in the Methods section.

By incorporating opto-electric feedback circuits in the two loops, we can introduce effective Kerr nonlinearity into the temporal lattice. An opto-electric feedback circuit mainly consists of an optical coupler (OC), a photodiode (PD), an amplifier (AMP), and a phase modulator (PM). The OC separates a minor part of light pulse train out of the fiber loop. The PD and subsequent AMP transfers the optical pulse sequence into electric signal with considerable amplitude. By applying the electric signal on the

PM, the optical pulse train will acquire an additional phase modulation. Such a modulation is directly proportional to the intensity profile of light signal, thus resembling the phase shift induced by the Kerr nonlinearity. Besides, the real-time response on light signal is also mimicked to fully emulate the Kerr nonlinearity (see [Methods](#)). Quantitatively, the effective Kerr nonlinear coefficient in our scheme can be calculated as $\kappa = \pi G_e R G_o I / V_\pi$, where I is the light intensity before the OC, G_o and G_e are the optical power gain factor and voltage gain factor of feedback circuit, R is the voltage responsivity of PD, and V_π is the half-wave voltage of PM. One sees that the effective Kerr coefficient can be readily modified by changing the optical/electric losses of passive devices or gain factor of AMP. Besides, our nonlinear loop circuit is actually operated at certain mw light power and gets rid of the natural optical nonlinearity. These peculiar properties are quite desirable in nonlinear optics and enable highly flexible control of nonlinear effect.

Theoretical model. The pulse dynamics in the Kerr nonlinear NH temporal lattice realizes a one-dimensional nonlinear quantum walk, which is described by the following discrete-time set of coupled wave equations^{10,15,25-27}

$$\begin{cases} u_n^{m+1} = e^{-\gamma} [\cos(\beta)u_{n+1}^m + i \sin(\beta)v_{n+1}^m] e^{i\chi |e^{-\gamma} [\cos(\beta)u_{n+1}^m + i \sin(\beta)v_{n+1}^m]|^2} \\ v_n^{m+1} = e^{+\gamma} [i \sin(\beta)u_{n-1}^m + \cos(\beta)v_{n-1}^m] e^{i\chi |e^{+\gamma} [i \sin(\beta)u_{n-1}^m + \cos(\beta)v_{n-1}^m]|^2} \end{cases}, \quad (1)$$

where u_n^m and v_n^m represent the pulse amplitudes in the short and long loops normalized by the square root of total intensity of incident pulses I_0 , and β determines the coupling ratio of VOC in the form of $\sin^2\beta/\cos^2\beta$. The variable χ denotes the Kerr coefficient defined for the normalized pulse amplitudes, which reads $\chi = \pi G_e R G_o I_0 / V_\pi$. We focus our study mostly to a lattice with OBC. In this case, at the left and right boundaries, the evolution equations in even steps read

$$\begin{cases} v_{-N}^{m+1} = i e^\gamma u_{-(N-1)}^m e^{i\chi |i e^\gamma u_{-(N-1)}^m|^2}, & \text{left boundary} \\ u_N^{m+1} = i e^{-\gamma} v_{N-1}^m e^{i\chi |i e^{-\gamma} v_{N-1}^m|^2}, & \text{right boundary} \end{cases}, \quad (2)$$

whereas at odd steps the pulse dynamics at boundaries could be calculated by Eq. (1). As shown in [Supplementary Note 1](#), the nonlinear quantum walk described by Eq. (1) realizes the nonlinear Hatano-Nelson model^{16,20,22} when the coupling angle β is close to $\pi/2$ and the nonlinearity is weak. Hence, we expect our model to sustain nonlinear skin solitons and to show competition between skin localization

and nonlinear localization in the bulk^{20,22}.

To calculate the nonlinear eigenvalues and eigenmodes under OBC, we derive the two-step propagator U of temporal lattice from Eqs. (1) and (2). Specifically, the propagator U can be denoted by the dot product of a linear part U_L and a nonlinear part U_{NL} , i.e., $U = U_L \cdot U_{NL}$, as detailed in [Supplementary Note 2](#). With $|\psi(m)\rangle = (v_{-N}^m \ u_{-N}^m \ v_{-(N-2)}^m \ u_{-(N-2)}^m \ \dots \ v_{N-2}^m \ u_{N-2}^m \ v_N^m \ u_N^m)^T$ being the vector of the wave amplitudes, the two-step evolution reads

$$|\psi(m+2)\rangle = U |\psi(m)\rangle. \quad (3)$$

We can introduce the nonlinear eigenmodes $|\Psi\rangle$ and corresponding nonlinear eigenvalues, i.e., the propagation constant or quasi energy θ , via the nonlinear eigen equation

$$U |\Psi\rangle = e^{i\theta} |\Psi\rangle, \quad (4)$$

where $|\Psi\rangle = (v_{-N} \ u_{-N} \ v_{-(N-2)} \ u_{-(N-2)} \ \dots \ v_{N-2} \ u_{N-2} \ v_N \ u_N)^T$. In the linear case, only the linear part U_L exists, thereby $|\Psi\rangle$ and θ could be directly obtained through solving the linear eigen equation $U_L |\Psi\rangle = e^{i\theta} |\Psi\rangle$. In the nonlinear case, the nonlinear part U_{NL} needs to be considered, and the intensity profile of eigenmode can inversely determine the phases within U_{NL} . The eigenmode is therefore a self-consistent solution of the nonlinear eigen equation (4). While under periodic boundary condition the nonlinear eigenfunctions are still plane waves and the Kerr nonlinearity just produces a shift of spectrum along the real energy axis as compared with the linear case, under OBC nonlinearity induces strong reshaping of nonlinear eigenmodes. To handle this nonlinear problem, we implement the self-consistent iteration algorithm and numerically calculate the eigenmode²⁸ (see [Methods](#)). We mention that, via the non-unitary gauge transformation $u_n^m \rightarrow u_n^m \exp(\gamma n)$ and $v_n^m \rightarrow v_n^m \exp(\gamma n)$, under OBC the NH terms can be removed from Eq. (1), the dynamics becomes conservative which implies that the nonlinear eigenvalue θ can be real under OBC. However, the competition of Kerr self-trapping and NHSE induces consistent reshaping of nonlinear eigenmodes. To reveal how the nonlinearity influence the localization strength of eigenmode, we calculate the inverse participation ratio (IPR) of mode profile²⁹, which reads

$$\text{IPR} = \frac{\sum_n (|u_n|^2 + |v_n|^2)^2}{\left[\sum_n (|u_n|^2 + |v_n|^2) \right]^2}. \quad (5)$$

The IPR varies in the range $(0, 1]$, with IPR close to zero for extended states and IPR close to one for tightly localized states. A larger IPR reflects a higher degree of localization of the eigenmode. We also

mention that, in the linear or weakly nonlinear regime, using the bulk band structure could efficiently describe the NHSE dynamics in bulk, which manifests as an unidirectional amplifying transport (see [Supplementary Note 3](#)).

Localization enhancement of nonlinear NHSE. To elucidate the influence of Kerr nonlinearity on NHSE, we comprehensively compare the mode profiles, propagation constants, and IPR of linear and nonlinear skin modes in [Fig. 2](#). The lattice sites range from $n = -10$ to $n = 10$, the gain/loss parameter is set as $\gamma = 0.2$, and the coupling angle is chosen as $\beta = \pi/3$. In the linear case ([Fig. 2a](#)), all skin modes localize near the right edge $n = 10$, and their propagation constants are within the real part of the bulk band structure. Besides, the above propagation constants are entirely real, which is starkly contrast to the complex bulk band structure (see [Supplementary Note 4](#)). Such localized behaviors of eigenmodes and deviation of spectrum evidently demonstrate the existence of NHSE. However, these skin modes widely distribute from $n = 0$ to $n = 10$. And the average IPR is calculated as 0.35 based on the averaged intensity profile of all skin modes, which indicates a relatively weak localization. To confirm the above analysis, we simulate and measure the propagation of the most localized skin mode, i.e., the 6th mode labeled by the blue color in [Fig. 2a](#). In the experiment, the linear skin mode is prepared by carefully applying intensity, phase, and coupling modulations in the process of single pulse diffraction. As shown in [Figs. 2b](#) and [2c](#), the experimental result coincides quite well with the simulated one. The skin mode stably evolves with an unchanged profile and localizes near the right edge.

The nonlinear skin modes can exhibit different properties compared with the linear ones^{16,20,22}. Using the self-consistent iteration algorithm, we can obtain two stable nonlinear skin modes at the right edge, i.e., the mode 1 and 2, in which the optical energy is mainly concentrated in the long and short loops, respectively. Such modes can be regarded as edge skin solitons²², where the skin effect and self-trapping cooperatively offer strong localization at the right boundary. As depicted in [Fig. 2d](#), the mode profile is remarkably compressed compared to the linear skin mode. This is because the Kerr nonlinear phase can form a nonlinear waveguide^{30,31}, which can further confine the localized linear skin mode. More interestingly, the nonlinear waveguide can lift the propagation constant into the gap of bulk band structure. Akin to the topological edge state, the nonlinear skin mode is hard to couple with the bulk modes and thus shows highly localized behaviors^{26,32,33}. The IPR enhancement also supports the above analysis. At the edge of band gap (corresponding to very weak or strong nonlinearity), we fail to search

a stable skin mode with high localization considering the closeness to the bulk bands^{32,33}. As illustrated in Figs. 2e and 2f with $\chi = 0.4\pi$, the intensity evolution is well confined within the two rightmost sites at every step, and the mode profile periodically revives after each two steps. For the nonlinear skin mode 2, the mode profile becomes extremely localized and even distributes within nearly a single site, as shown in Figs. 2g to 2i. This is because the sublattice corresponding to the short loop at $n = 10$ is exactly the right boundary of lattice, and the reflection at boundary can further confine the mode profile. In summary, the Kerr nonlinearity can remarkably enhance the localization of NHSE at the preferred edge and generate highly confined skin modes.

Robustness enhancement of nonlinear NHSE. To examine the concerned robustness of NHSE^{10,34}, we impose transverse random phase noise $\alpha(n)$ onto the skin mode evolutions shown in Fig. 2. The phase noise ranges from $-\Delta\alpha/2$ to $\Delta\alpha/2$ with $\Delta\alpha$ being the noise strength. Figures 3a to 3c illustrate the experimental evolutions of the 6th linear skin mode and the nonlinear skin mode 1 and 2, in which the noise strength is chosen as $\Delta\alpha = 0.25\pi$. In the linear case, one sees that the skin mode still localizes around the right boundary. Nevertheless, its intensity pattern is severely distorted by the phase disorder, accompanied with irregular energy amplification and attenuation during evolution. For the nonlinear skin mode 1, only a small amount of distortion is observed. Remarkably, for the nonlinear skin mode 2, its evolution is even immune to the disorder. The reason is that the formed nonlinear waveguide makes the mode propagation constant locate at the center of band gap and thus gives rise to very strong robustness. The suppressed intensity distortion at the right edge $n = 10$ (Figs. 3d to 3f) also confirms the enhanced robustness of nonlinear NHSE.

Nonlinear suppression of NHSE and bulk skin solitons. At the right boundary, the Kerr nonlinear NHSE is demonstrated to be a powerful localization mechanism since the NHSE and Kerr self-trapping can reinforce each other. However, in the bulk or at the left edge, the NHSE manifests as a rightward transport instead of localization and competition with the Kerr self-trapping arises. Here we show that such a competition can lead to a total suppression of NHSE and thus yields bulk skin solitons²² away from the right edge. As shown in Fig. 4a, the bulk mode also has a highly confined, albeit asymmetric, profile with its propagation constant locating in the band gap. The threshold of nonlinearity for the formation of bulk skin soliton is clearly raised compared to the nonlinear skin modes at the right edge.

As illustrated in Figs. 4b and 4c with $\chi = 0.5\pi$, a stable mode propagation can be observed in the bulk, evidently demonstrating the nonlinear suppression of NHSE. Considering the translation invariance of temporal lattice, the bulk modes with same characteristics can also be formed around other sites in the bulk. More interestingly, we can even obtain a localized eigenmode at the left edge, as plotted in Fig. 4d. Owing to the edge reflection, the threshold for existence of this mode is further increased, and the mode profile is slightly compressed. The simulation and experiment displayed in Figs. 4e and 4f clearly support the validity of nonlinear left-edge mode.

Tunable light router based on nonlinearity-controlled NHSE. We have unveiled that the localized eigenmodes can be established around each site of lattice thanks to the nonlinear enhancement and suppression of NHSE, while unidirectional transport toward the boundary, robust against disorder, is allowed in the linear or weakly nonlinear regime, i.e., when the pulse intensity is low enough. By using the mode formation around different sites, here we ingeniously design a nonlinear optical router with its output position flexibly tuned by the nonlinear strength. Specifically, a single weak pulse is adopted to excite a lattice site away from the right edge. For different nonlinear coefficients, the pulses move along different routing trajectories (Fig. 5a). Figure 5b plots the simulated intensity distribution, center of mass n_{out} , and IPR of output pulse sequence varying with the nonlinear coefficient χ . Here, the pulse is injected at $n = 4$, and its evolution lasts 30 steps. When χ increases from 0.15π to 0.6π , a leftwards motion of pulse train from $n_{\text{out}} = 9.7$ to $n_{\text{out}} = 4.5$ can be clearly observed at the output plane, with the intensity profile of pulse train well localized. However, from the linear to weakly nonlinear realms, the output pulse train shows a broadened intensity profile, and the performance of router is degraded. This is because the edge can reflect light pulses into bulk, but the Kerr nonlinearity is not strong enough to suppress the reflection and confine these pulses. For $\chi > 0.6\pi$, we also cannot get the optimal routing performance, which is mainly caused by the instability of nonlinear mode (see Supplementary Note 5). Figures 5d and 5e display the measured routing processes for $\chi = 0.15\pi$ and 0.6π , with Fig. 5c being a comparison in the linear case, which clearly demonstrate routing application. In addition, the routing towards other ports are illustrated in Supplementary Note 6. Note that, the above pulse sequences with high localization are not strictly the nonlinear eigenmodes, but they exhibit a similar evolution behavior.

Discussion

In conclusion, we reported the first experimental demonstration of nonlinear NHSE and skin solitons, unveiling the intriguing competition or cooperation of linear NHSE and nonlinear self-trapping. Our experiment utilizes temporal quantum-walk optical lattices incorporated with opto-electric feedbacks, providing a highly alternative platform to realize the Kerr nonlinearity with a high degree of tunability. At the preferred boundary, i.e., the right boundary here, the linear NHSE and nonlinear self-trapping cooperate due to the formation of nonlinear waveguide, yielding extremely localized nonlinear skin modes (edge skin solitons). Furthermore, under phase disorder, edge skin solitons are demonstrated to have highly enhanced robustness compared with the linear case. More surprisingly, in the bulk or at the left boundary, the NHSE can be entirely suppressed as the Kerr self-trapping is strong enough to overcome the NHSE-induced transport, leading to the formation of bulk or left-edge skin solitons. By exploiting the nonlinearity-controlled NHSE, we strategically design and experimentally demonstrate a light router with its output position efficiently controlled by the nonlinear strength.

Our work pushes the celebrated NHSE into the nonlinear realm, providing a bridge between the NH topology and nonlinear physics. Our results could significantly influence practical applications, creating a unique pathway for applying nonlinear NH skin physics to robust light signal transmission, routing, and processing. This development could play a key role in advancing the next-generation light communication systems. The low optical power requirement and high tunability of our artificial Kerr nonlinearity will profoundly boost the development of basic nonlinear devices for optical computation, including coupler^{35,36}, switch^{37,38}, and interferometer^{39,40}. Finally, we mention that using our nonlinear temporal lattice, the interplays of nonlinearity and other important physical effects could be envisaged, including Landau-Zener tunneling^{41,42}, ac-driven dynamic localization^{29,43}, time refraction⁴⁴⁻⁴⁶, and Anderson localization^{47,48}.

Methods

Experimental setup. Extended Data Fig. 1 displays the experimental setup. The averaging length and length difference of two loops are chosen as ~ 5 km and ~ 0.3 km, corresponding to time delays of $T \approx 25$ μ s and $2\Delta T \approx 1.5$ μ s, respectively. The width of input pulse is set as ~ 0.8 μ s to avoid the overlapping between the pulses at adjacent lattice sites. The initial optical pulse is produced through modulating a 1555 nm continuous-wave light beam with a Mach-Zehnder modulator (MZM), and the MZM is driven by the electric pulse from an arbitrary waveform generator (AWG). The pulse is injected into the long loop through an optical switch (OS). During the circulations in the dual-loop circuit, the optical loss is compensated by erbium-doped fiber amplifiers (EDFAs). To get rid of the transient of EDFA, the signal pulse is combined with a strong pilot light operated at a wavelength of 1538 nm. Employing band-pass filters (BPFs), the pilot light and spontaneous emission noise are soon removed. In order to capture the evolving pulses, we couple the optical signals out of the loops and record them by photodiodes (PDs) and subsequent oscilloscopes (OSCs). The polarization states of pulses are controlled and monitored through polarization controllers (PCs) and polarization beam splitter (PBS).

To realize the nonreciprocal hoppings essential for NHSE, we introduce loss/gain modulation into the two loops. Specifically, in the short loop, we make the light gain from EDFA smaller than the total loss induced by other passive devices. The pulse thus experiences a lossy circulation in the short loop, hence yielding a lossy leftwards hopping in the temporal lattice. Meanwhile, in the long loop, the gain is larger than the total loss, leading to a amplified rightwards hopping. The nonreciprocal hoppings can hence be introduced into the temporal lattice. Here the total losses of fiber loops are controlled by the acousto-optic modulators (AOMs), which are driven by AWGs and can impose arbitrary-form intensity modulations onto the light pulses.

To realize the Kerr nonlinearity, here we utilize opto-electric feedback circuits in the coupled fiber loops. In the opto-electric feedback circuit (labeled by orange wire), the OC partly couples the optical pulses out of the loop. The PD and subsequent AMP convert the light pulses into electric signal, which is then imposed on the original pulses by the PM. Such a phase modulation can resemble the intensity-dependent phase shift induced by the Kerr nonlinearity. Apart from the intensity dependence, another key ingredient to emulating the nonlinearity is the real-time response on light signal. Conventionally, in a continuous medium where the optical field continuously evolves with time, an ultra-fast response

speed is usually required. In contrast, our temporal lattice holds a discrete evolution along the time step m labelled by each circulation. We can achieve the real-time response even with a long time delay provided that the feedback is within the same circulation. Here, there is indeed a time delay between the original light signal at the OC and the feedback at the PM. And we need to insert a haul of single-mode fiber (SMF) into the feedback circuit to compensate the time delay and make the feedback phase perfectly aligned with the delayed optical signal. In addition, the VOC in the feedback circuit serves as an intensity modulator to switch on/off the Kerr nonlinearity and tune the nonlinear coefficient.

Construction of OBC. To realize the OBC required for NHSE, here we modulate the coupling in the temporal lattice. Notably, we only need to switch the coupling in odd steps considering the quantum walk nature of temporal lattice. Like the quantum walk, the pulse can merely hop to two adjacent sites in a single step. When we switch the coupling ratio to $1/0$ at the left boundary of each odd step, i.e., at $n = -(N+1)$, the pulse can only move to the site $n = -N$ in the next even step. In the next coupling, although without coupling switch, the pulse can only be coupled to the sites $n = -(N+1)$ and $n = -(N-1)$, which are still within the left boundary. Meanwhile, to set the right boundary, we switch the coupling ratio at $n = N+1$ into $1/0$ in each odd step. Note that, at the site $n = -(N+1)$ of odd steps, the optical pulse exists only in the short loop since the pulse in the long loop should come from the site $n = -(N+2)$ of last even step, which has extended the lattice boundary. Similarly, at the site $n = N+1$ of odd steps, the pulse exists only in the long loop.

Self-consistent iteration algorithm. To numerically find the stable nonlinear eigenmode that localizes around a certain site, here we utilize the self-consistent iteration algorithm. A localized Gaussian wave packet centering around a certain site is first assumed with the total intensity set as unity. Considering a chosen Kerr coefficient χ , we can calculate the nonlinear phase shifts within the propagator U . By solving the eigen equation (4), a series of nonlinear eigenmodes are temporally obtained, and the most localized one is chosen as the initial state of next iteration. Note that, the total intensity is kept fixed through a normalization operation. After numerous iterations, a self-consistent solution can be obtained when the mode profile in present iteration is identical with the one in last iteration. The final calculated eigenvalue is the propagation constant of nonlinear eigenmode. To exclude the unstable solution, we finally inject the calculated eigenmode into the temporal lattice and summate the intensity variations

at all sites after propagating 100 steps. As the summation is more than 10% of the total intensity, the nonlinear eigenmode is regarded as unstable. It should be noted that, the solution obtained from self-consistent iteration algorithm relies on the choice of initial iteration state. For different initial iteration states respectively concentrated in the short and loops, we could acquire different eigenmode solutions, e.g., the nonlinear skin mode 1 and 2. When the central position of initial iteration state is shifted, the eigenmode solution also changes, e.g., the skin and bulk modes. For other profiles of initial iteration state rather than Gaussian packet, we may also find different solutions. Considering such a complexity of solving the nonlinear eigen equation, this study may omit some other possible eigenmode solutions, but the present results have already demonstrated the powerful control of NHSE based on the interplay of non-Hermiticity and Kerr nonlinearity.

Data availability

All the data supporting this study are available in the paper and Supplementary Information. Additional data related to this paper are available from the corresponding authors upon request.

References

1. Bender, C. M. & Boettcher, S. Real spectra in non-Hermitian Hamiltonians having PT symmetry. *Phys. Rev. Lett.* **80**, 5243-5246 (1998).
2. Kawabata, K., Shiozaki, K., Ueda, M. & Sato, M. Symmetry and topology in non-Hermitian physics. *Phys. Rev. X* **9**, 041015 (2019).
3. Ashida, Y., Gong, Z. & Ueda, M. Non-Hermitian physics. *Adv. Phys.* **69**, 249-435 (2020).
4. Bergholtz, E. J., Budich, J. C. & Kunst, F. K. Exceptional topology of non-Hermitian systems. *Rev. Mod. Phys.* **93**, 015005 (2021).
5. Yao, S. & Wang, Z. Edge states and topological invariants of non-Hermitian systems. *Phys. Rev. Lett.* **121**, 086803 (2018).
6. Yokomizo, K. & Murakami, S. Non-Bloch band theory of non-Hermitian systems. *Phys. Rev. Lett.* **123**, 066404 (2019).
7. Okuma, N., Kawabata, K., Shiozaki, K. & Sato, M. Topological origin of non-Hermitian skin effects. *Phys. Rev. Lett.* **124**, 086801 (2020).
8. Zhang, X., Zhang, T., Lu, M.-H. & Chen, Y.-F. A review on non-Hermitian skin effect. *Adv. Phys. X* **7**, 2109431 (2022).
9. Lin, R., Tai, T., Li, L. & Lee, C. H. Topological non-Hermitian skin effect. *Front. Phys.* **18**, 53605 (2023).
10. Weidemann, S. *et al.* Topological funneling of light. *Science* **368**, 311-314 (2020).
11. McDonald, A. & Clerk, A. A. Exponentially-enhanced quantum sensing with non-Hermitian lattice dynamics. *Nat. Commun.* **11**, 5382 (2020).
12. Yuan, H. *et al.* Non-Hermitian topoelectrical circuit sensor with high sensitivity. *Adv. Sci.* **10**, 2301128 (2023).
13. Xiao, L. *et al.* Non-Hermitian bulk-boundary correspondence in quantum dynamics. *Nat. Phys.* **16**, 761-766 (2020).
14. Lin, Q., Yi, W. & Xue, P. Manipulating directional flow in a two-dimensional photonic quantum walk under a synthetic magnetic field. *Nat. Commun.* **14**, 6283 (2023).
15. Weidemann, S., Kremer, M., Longhi, S. & Szameit, A. Topological triple phase transition in non-Hermitian Floquet quasicrystals. *Nature* **601**, 354-359 (2022).
16. Yuce, C. Nonlinear non-Hermitian skin effect. *Phys. Lett. A* **408**, 127484 (2021).
17. Ezawa, M. Dynamical nonlinear higher-order non-Hermitian skin effects and topological trap-skin phase. *Phys. Rev. B* **105**, 125421 (2022).
18. Zhang, Z.-X. *et al.* Topological skin modes and intensity amplification in a nonlinear non-

- Hermitian lattice. *Phys. Rev. B* **108**, 125402 (2023).
19. Leefmans, C. R. *et al.* Topological temporally mode-locked laser. *Nat. Phys.* **20**, 852-858 (2024).
 20. Manda, B. M., Carretero-González, R., Kevrekidis, P. G. & Achilleos, V. Skin modes in a nonlinear Hatano-Nelson model. *Phys. Rev. B* **109**, 094308 (2024).
 21. Veenstra, J. *et al.* Non-reciprocal topological solitons in active metamaterials. *Nature* **627**, 528-533 (2024).
 22. Komis, I., Musslimani, Z. H. & Makris, K. G. Skin solitons. *Opt. Lett.* **48**, 6525-6528 (2023).
 23. Eisenberg, H. S., Silberberg, Y., Morandotti, R., Boyd, A. R. & Aitchison, J. S. Discrete spatial optical solitons in waveguide arrays. *Phys. Rev. Lett.* **81**, 3383-3386 (1998).
 24. Morandotti, R., Eisenberg, H. S., Silberberg, Y., Sorel, M. & Aitchison, J. S. Self-focusing and defocusing in waveguide arrays. *Phys. Rev. Lett.* **86**, 3296-3299 (2001).
 25. Wimmer, M. *et al.* Optical diametric drive acceleration through action-reaction symmetry breaking. *Nat. Phys.* **9**, 780-784 (2013).
 26. Wimmer, M. *et al.* Observation of optical solitons in PT-symmetric lattices. *Nat. Commun.* **6**, 7782 (2015).
 27. Marques Muniz, A. L. *et al.* Observation of photon-photon thermodynamic processes under negative optical temperature conditions. *Science* **379**, 1019-1023 (2023).
 28. Mitchell, M., Segev, M., Coskun, T. H. & Christodoulides, D. N. Theory of self-trapped spatially incoherent light beams. *Phys. Rev. Lett.* **79**, 4990-4993 (1997).
 29. Wang, S. *et al.* High-order dynamic localization and tunable temporal cloaking in ac-electric-field driven synthetic lattices. *Nat. Commun.* **13**, 7653 (2022).
 30. Stegeman, G. I. & Segev, M. Optical spatial solitons and their interactions: Universality and diversity. *Science* **286**, 1518-1523 (1999).
 31. Regensburger, A. *et al.* Observation of defect states in PT-symmetric optical lattices. *Phys. Rev. Lett.* **110**, 223902 (2013).
 32. Sukhorukov, A. A. & Kivshar, Y. S. Discrete gap solitons in modulated waveguide arrays. *Opt. Lett.* **27**, 2112-2114 (2002).
 33. Pelinovsky, D. E., Sukhorukov, A. A. & Kivshar, Y. S. Bifurcations and stability of gap solitons in periodic potentials. *Phys. Rev. E* **70**, 036618 (2004).
 34. Longhi, S., Gatti, D. & Valle, G. D. Robust light transport in non-Hermitian photonic lattices. *Sci. Rep.* **5**, 13376 (2015).
 35. Jensen, S. The nonlinear coherent coupler. *IEEE J. Quantum Electron.* **18**, 1580-1583 (1982).
 36. Thylen, L., Wright, E. M., Stegeman, G. I., Seaton, C. T. & Moloney, J. V. Beam-propagation method analysis of a nonlinear directional coupler. *Opt. Lett.* **11**, 739-741 (1986).

37. Smith, S. D. Optical bistability, photonic logic, and optical computation. *Appl. Opt.* **25**, 1550-1564 (1986).
38. Arkhipova, A. A. *et al.* Observation of nonlinearity-controlled switching of topological edge states. *Nanophotonics* **11**, 3653-3661 (2022).
39. Jinno, M. & Matsumoto, T. Nonlinear Sagnac interferometer switch and its applications. *IEEE J. Quantum Electron.* **28**, 875-882 (1992).
40. Chekhova, M. V. & Ou, Z. Y. Nonlinear interferometers in quantum optics. *Adv. Opt. Photonics* **8**, 104-155 (2016).
41. Longhi, S. Non-Bloch-band collapse and chiral Zener tunneling. *Phys. Rev. Lett.* **124**, 066602 (2020).
42. Wang, S. *et al.* Photonic Floquet Landau-Zener tunneling and temporal beam splitters. *Sci. Adv.* **9**, eadh0415 (2023).
43. Dunlap, D. H. & Kenkre, V. M. Dynamic localization of a charged particle moving under the influence of an electric field. *Phys. Rev. B* **34**, 3625-3633 (1986).
44. Dong, Z. *et al.* Quantum time reflection and refraction of ultracold atoms. *Nat. Photonics* **18**, 68-73 (2023).
45. Ye, H. *et al.* Reconfigurable refraction manipulation at synthetic temporal interfaces with scalar and vector gauge potentials. *Proc. Natl. Acad. Sci.* **120**, e2300860120 (2023).
46. Qin, C. *et al.* Observation of discrete-light temporal refraction by moving potentials with broken Galilean invariance. *Nat. Commun.* **15**, 5444 (2024).
47. Weidemann, S., Kremer, M., Longhi, S. & Szameit, A. Coexistence of dynamical delocalization and spectral localization through stochastic dissipation. *Nat. Photonics* **15**, 576-581 (2021).
48. Dikopoltsev, A. *et al.* Observation of Anderson localization beyond the spectrum of the disorder. *Sci. Adv.* **8**, eabn7769 (2022).

Acknowledgements

The work is supported by the National Natural Science Foundation of China (No. 12374305, No. 62305122, No. 12474381, No. 12021004, No. 12204185 and No. 62375097) and the Natural Science Foundation of Hubei Province (No. 2022CFB036). S.L. acknowledges the Spanish Agencia Estatal de Investigacion (MDM-2017-0711).

Author contributions

B.W. conceived the idea. S.W. and C.L. designed and performed the experiment. S.W., C.Q., and B.W. analysed the data. S.L. and B.W. provided the theoretical support. B.W. and P.L. supervised the project. All authors contributed to the discussion of the results and writing of the manuscript.

Competing interests

The authors declare no competing interests.

Additional information

Supplementary information accompanies this paper at <https://doi.org/xxxxx/xxxxx>.

Figures and captions

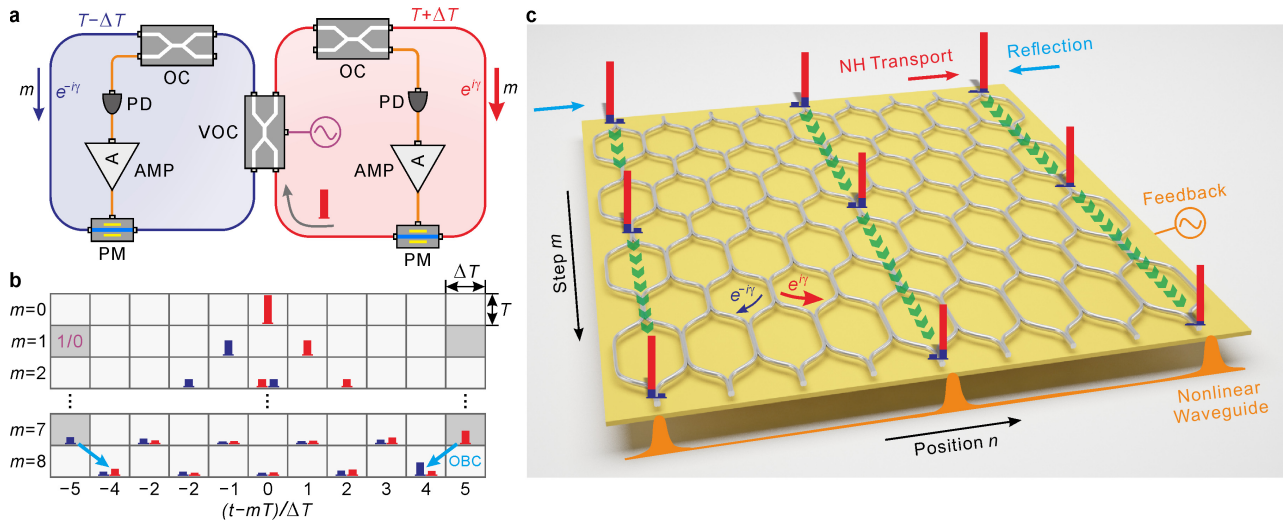


Fig. 1. Construction of Kerr nonlinear NH temporal lattices under OBC. **a** Schematic diagram of two coupled fiber loops incorporated with opto-electric feedbacks. The two loops possess slight length difference and are bridged by a VOC, in which the pulse circulation resembles the wave dynamics in a temporal quantum-walk lattice. The incorporated opto-electric feedback circuit consists of an OC, a PD, an AMP, and a PM. Such a configuration can couple the pulses out of the loops and interprets their intensity profile as phase modulation onto the original pulses, hence mimicking Kerr nonlinearity. The loss and gain in the short and long loops generate nonreciprocal hoppings in the temporal lattice. The dynamical switch of the ratio of VOC yields the OBC. **b** Construction principle of temporal quantum-walk lattice based on time multiplexing of optical pulse. **c** Schematic of temporal quantum-walk lattice supporting NHSE. In the linear lattice, a rightwards NH transport and edge reflection simultaneously exist, and the balance of the two effects form stable skin modes at the right boundary. The opto-electric feedback imposes on-site intensity-dependent phase modulation at each lattice site (m, n) , which can generate nonlinear waveguides in the synthetic lattice and further engineer the NH dynamics and the profiles of eigenmodes.

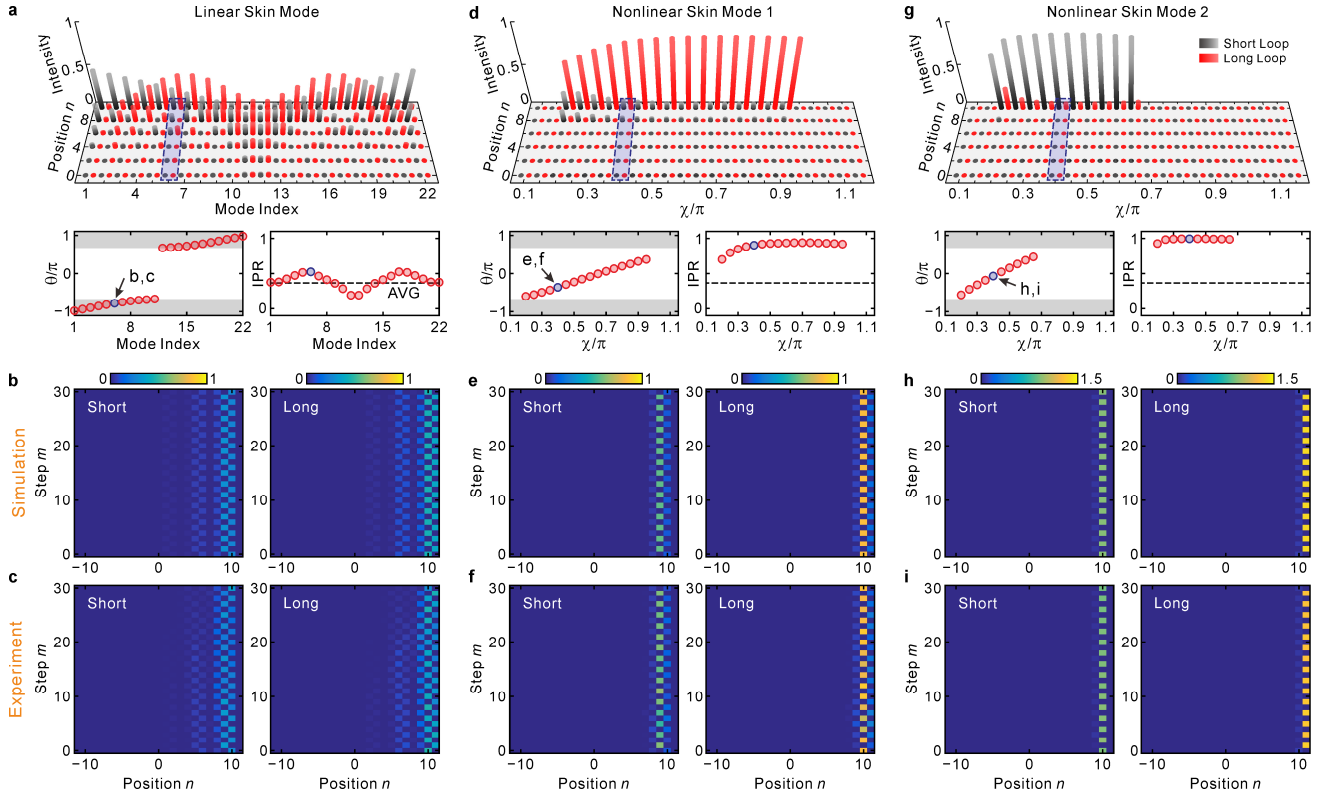


Fig. 2. Localization enhancement of nonlinear skin modes. **a** Mode profiles, eigenvalue spectrum, and IPR of linear skin modes. The black and red bars in mode profile subplot correspond to the short and long loops, respectively. The gray zones in spectrum indicate the real parts of bulk band structure, and the open circles correspond to the skin modes. The dashed line in the IPR subplot denote the IPR of the averaging intensity of all skin modes, which can reflect the localization strength of linear NHSE. **b, c** Simulated and measured pulse intensity evolutions of the 6th linear skin mode. **d** Mode profiles, eigenvalue spectrum, and IPR of nonlinear skin mode 1 varying with Kerr coefficient χ . **e, f** Simulated and measured pulse intensity evolutions of nonlinear skin mode 1 at $\chi = 0.4\pi$. **g-i** correspond to the nonlinear skin mode 2.

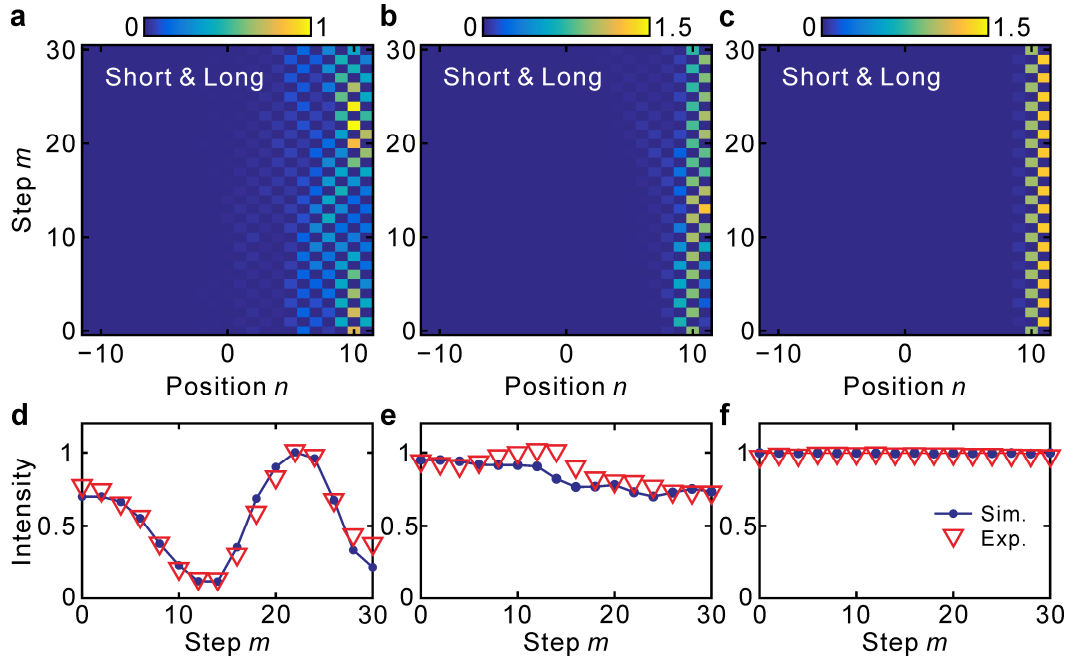


Fig. 3. Robustness enhancement of nonlinear skin modes. **a** Measured pulse intensity evolution of the 6th linear skin mode in the presence of random phase disorder. The disorder strength is set as $\Delta\alpha = 0.25\pi$. **b, c** Measured pulse intensity evolutions of nonlinear skin mode 1 and 2 under phase disorder. **d-f** Pulse intensity evolutions at $n = 10$ for the 6th linear skin mode and nonlinear skin mode 1 and 2, respectively. The blue dots and red triangles denote the simulated and measured results, respectively.

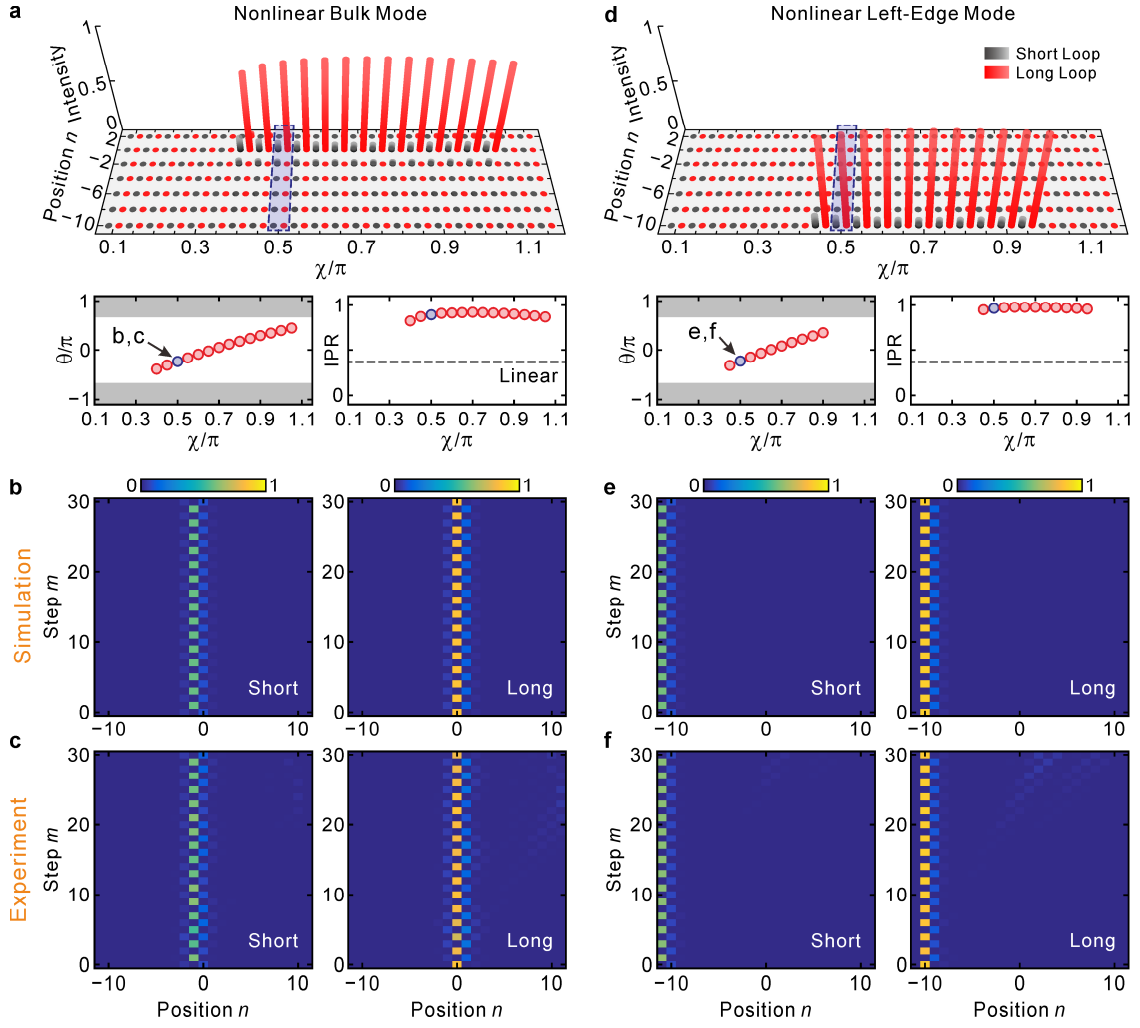


Fig. 4. Nonlinear suppression of NHSE in bulk and left edge. **a** Mode profiles, eigenvalue spectrum, and IPR of nonlinear bulk mode versus Kerr coefficient χ . **b, c** Simulated and measured pulse intensity evolutions of nonlinear bulk mode at $\chi = 0.5\pi$. **d-f** correspond to nonlinear left-edge mode.

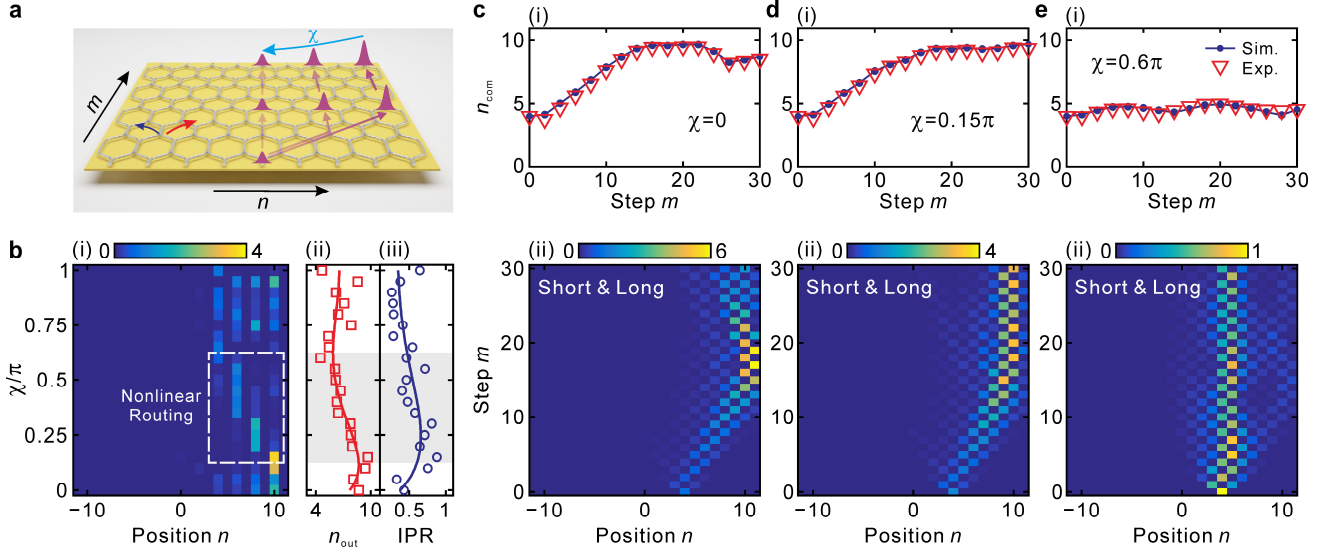
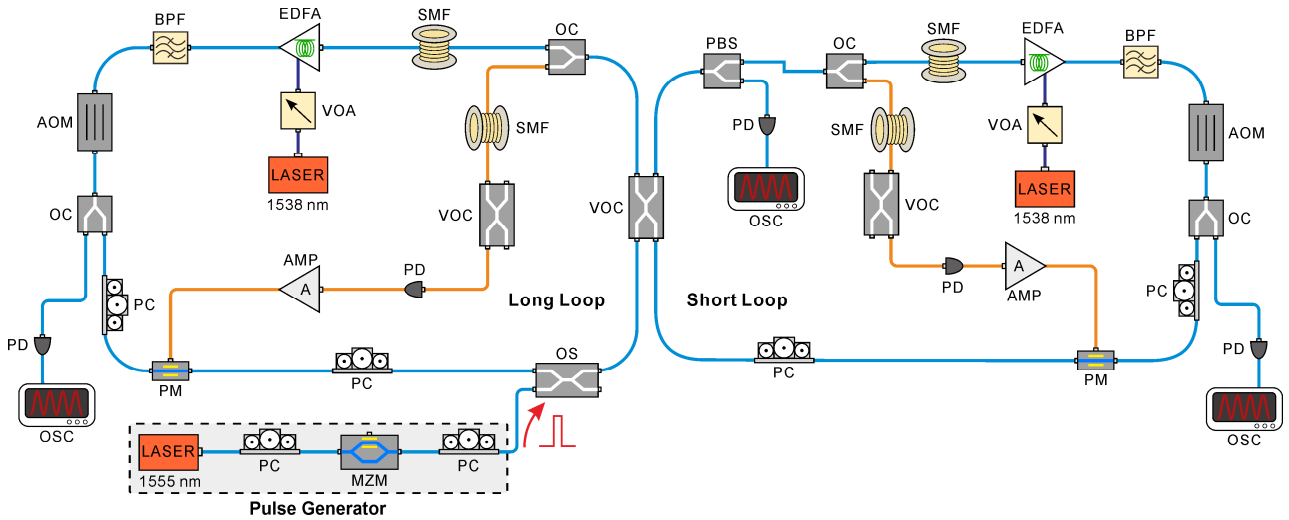


Fig. 5. Optical router based on nonlinearity-controlled NHSE. **a** Schematic of nonlinear router, in which the left, central, and right trajectories correspond to the routings for large, moderate, and small Kerr coefficient χ , respectively. The varying transparency of trajectory indicates the intensity evolution of the wave packet. For a small nonlinear coefficient χ , the optical pulses first move towards the right boundary accompanied with exponentially increasing intensities. When approaching the boundary, the amplified pulses can yield strong enough Kerr nonlinearity and forms nonlinear skin modes. A robust routing is therefore generated. For a moderate χ , the mode formation requires lower intensity and hence a shorter amplifying rightward transport. The routing will be shifted from the right boundary into the bulk. For a large enough χ , the skin soliton could be formed as soon as the pulse is injected, leading to a routing around initial position. **b** Simulated intensity distribution (i), center of mass n_{out} (ii), and IPR (iii) of pulse sequence at output plane varying with Kerr coefficient χ . In (ii) and (iii), the solid curves are the fitting results based on the simulation, which reflect the tendencies of simulated results. Here, the initial pulse locates at $n = 4$ and is injected into the long loop. **c-e** Evolutions of center of mass n_{com} (i) and measured pulse intensities (ii) for $\chi = 0, 0.15\pi$, and 0.6π , respectively.



Extended Data Fig. 1. Experimental Setup. The left and right parts represent the long and short loops, respectively. All optical and electric components are as follows: Polarization controller (PC), Mach-Zehnder modulator (MZM), optical switch (OS), variable optical coupler (VOC), optical coupler (OC), single-mode fiber (SMF), erbium-doped fiber amplifier (EDFA), variable optical attenuator (VOA), band-pass filter (BPF), acousto-optic modulator (AOM), photodiode (PD), oscilloscope (OSC), phase modulator (PM), amplifier (AMP), polarization beam splitter (PBS).